We are IntechOpen, the world's leading publisher of Open Access books Built by scientists, for scientists

4,800
Open access books available

122,000
International authors and editors

135M
Downloads

Our authors are among the

154
Countries delivered to

TOP 1%
most cited scientists

12.2%
Contributors from top 500 universities

WEB OF SCIENCE™

Selection of our books indexed in the Book Citation Index in Web of Science™ Core Collection (BKCI)

Interested in publishing with us?
Contact book.department@intechopen.com

Numbers displayed above are based on latest data collected.
For more information visit www.intechopen.com

15

Ultra-Wideband Pulse-Based Microwave Imaging for Breast Cancer Detection: Experimental Issues and Compensations

Joshua C. Y. Lai, Cheong Boon Soh, Kay Soon Low and Erry Gunawan
Nanyang Technological University
Singapore

1. Introduction

Recent research based on numerical modeling (Bond, 2003; Xu, 2001) that ignored hardware characteristics and simple experiments using homogenous breast phantoms (Sill, 2005; Xu, 2004) have shown the potential of ultra-wideband to detect early stage breast cancer. However, clutter interference from heterogeneous breast tissues and hardware characteristics like pulse jitter, finite dynamic range and precision for signal acquisition can severely degrade the detectability of breast tumors. This chapter discusses the experimental issues encountered and compensation methods used to improve the detectability of tumor.
In order to bridge the gap between numerical simulations and experiments, it is important to identify the experimental issues before conducting experiments with more realistic breast phantoms so that the source of imaging artifacts can be identified and compensated. An ideal imaging scenario is first created where the simple sum-and-delay algorithm (Xu, 2001) is working perfectly. In this ideal scenario, the breast phantom is round and symmetrical such that the averaging method can perfectly remove the skin reflection. The breast medium is homogeneous such that propagation of signal in the medium is constant with accurate delay time estimation. Skin is approximated by a single interface (air to breast phantom) because its thickness is small compared to UWB pulse width in space.
In this chapter, several important experimental issues are discussed.

- Impulse Generator – Pulse Jitter Artifact
- Real Time Oscilloscope – Limited Dynamic Range
- Breast Phantom Positioning Error – Ring Artifact
- Signal Loss Compensation – Noise Amplification
- Filtering and Correlation – Noise Reduction
- Averaging and Antenna Number – Signal SNR vs Image SNR

To facilitate the discussion, the experimental setup will first be described in the following subsection 1.1. Experiments discussed in this chapter are conducted in time domain using an impulse generator and a real-time oscilloscope.

1.1 Experimental setup

A breast phantom is fabricated using soy bean oil (ε_r = 2.6, σ = 0.05 S/m), contained in a cylindrical polypropylene container (diameter 16 cm, height 12 cm). Tumor is simulated

with a small cylindrical shape jelly (ε_r = 8, σ = 0.4 S/m) with 4 mm diameter and 1 cm length made of tissue-mimicking phantom material (Lazebnik, 2005).
The excitation signal is generated using the Picosecond Pulse Labs 3500D impulse generator, which produces gaussian pulses with full width at half maximum (FWHM) of 80 picoseconds. Agilent DSO81204B real-time oscilloscope with 40 GHz sampling rate is used for recording the backscattered signals from the breast phantom.
Thales UWB antennas (Chua, 2005) are used as the transmitter and receiver of the UWB signals. The antennas dimension is 3 cm width and 4 cm height. The antennas gain is 11 dB with azimuth beamwidth of 60 degrees and elevation beamwidth of 40 degrees. The antennas return loss measured with Agilent N5230A vector network analyzer is lower than -10 dB from 2.4 to 12 GHz.
Breast phantom is placed on a rotary stage with antennas scanning at the side to simulate the human breast in prone position. Breast phantom is rotated for 360 degrees relative to the stationary antennas to simulate a circular antenna array around the breast circumference. The overall experimental setup is shown in Figure 1.
The collected signals are processed with averaging method (Xu, 2001) to remove the signal artifacts, which includes incident pulse, boundary reflection and multipath. The processing is also known as calibration in the literature. Delay-and-sum beamforming (Xu, 2001) algorithm is used to generate the image as in confocal imaging technique. Breast image is formed by synthetically focusing the signals received from the antenna array to every point within the region of interest.

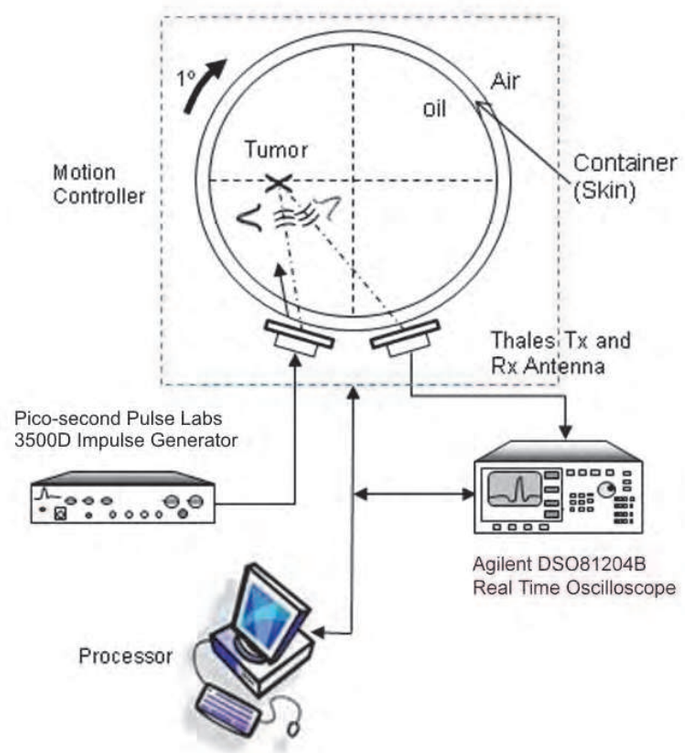

Fig. 1. Overall experimental setup.

2. Pulse jitter artifact and compensation

As mentioned in the introduction, averaging method is applied to remove artifacts in the received signals before delay-and-sum beamforming. An average of all received signals from different antennas is calculated. The averaged signal is used as a template artifact and is subtracted from individual received signals. Clean tumor responses can be obtained if the system is free of noise. The processing is also known as calibration in the literature.

However, averaging method will not work well if the received signals are not aligned perfectly and have unequal amplitudes. Pulse delay jitter is caused by the impulse generator being unable to maintain a constant delay time between trigger signal and the output UWB pulse. The maximum delay timing jitter measured with oscilloscope in the experiment is 31 ps. Pulse amplitude instability is caused by the impulse generator which is unable to maintain constant amplitude of the output UWB pulse.

Figures 2 and 3 show that pulse instability causes phase shift of 31 ps or 20 sample points in the signals. The resultant artifact would be large if the signals are not first compensated. For phase jitter compensation, all received signals are aligned by finding the zero-crossing point between maximum and minimum peaks and phase shifting the signals to the same zero-crossing point. For amplitude instability, compensation is done by normalizing all the signals peak-to-peak amplitude to one unit.

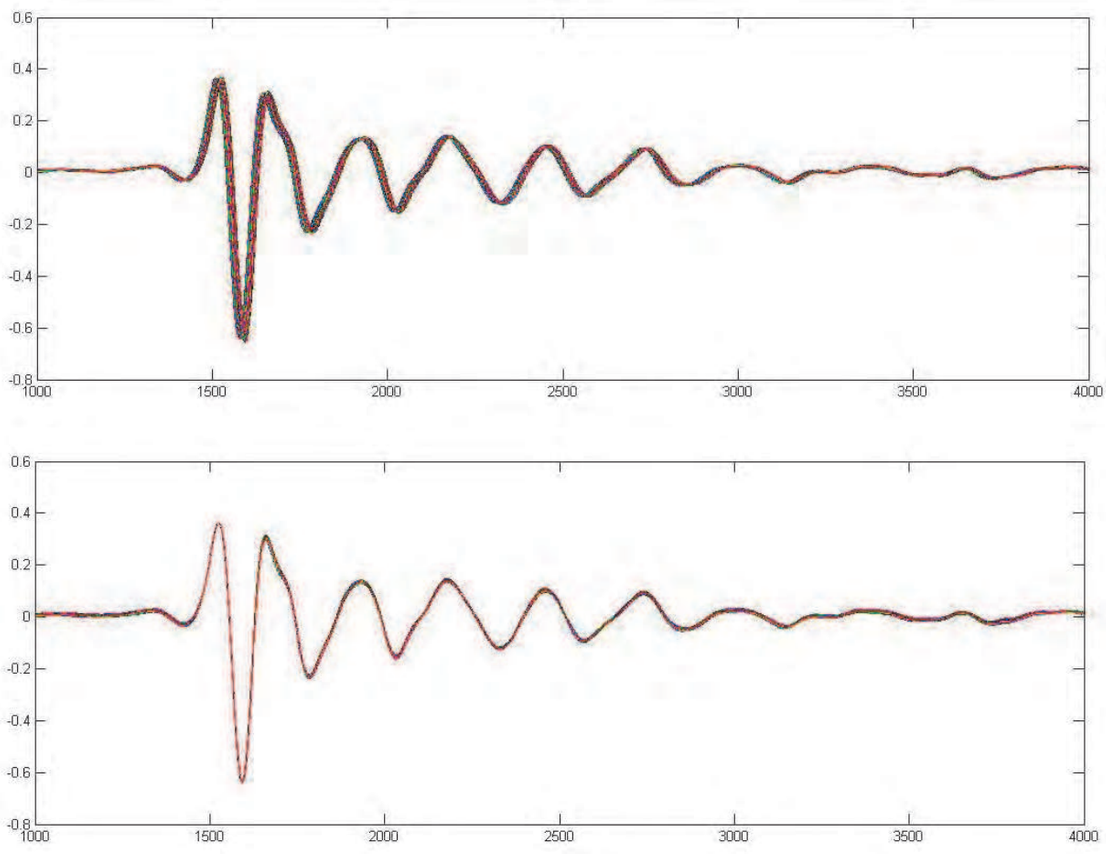

Fig. 2. Signals before and after pulse jitter compensation.

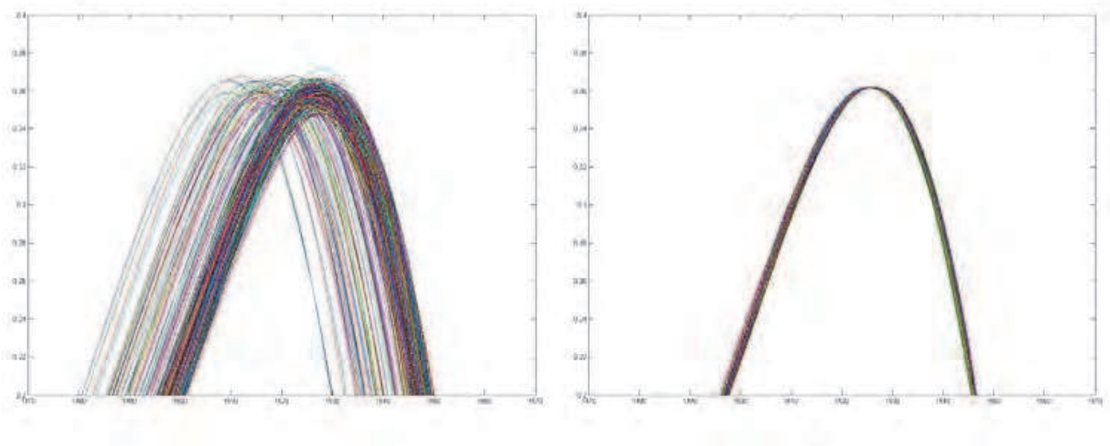

Fig. 3. Zoom in view of signals given in Figure 2.

To further minimize the phase error, the received signals are extrapolated to higher sampling rates. Table 1 shows the phase error for received signals and resultant signal artifact after pulse instability compensation at different extrapolated sampling rates. Measured noise amplitude is obtained after applying averaging method to a set of data collected from a tumor-free breast phantom. Simulated noise amplitude is calculated with Matlab by subtracting two identical signals, one signal is phase shifted by one sample time from another signal.

The noise amplitude shown in Table 1 is normalized to the incident pulse amplitude. The measured noise amplitude does not further decrease with higher sampling rates greater than 1 THz because the other contributors of noise such as environmental noise becomes significant, whereas the simulated noise amplitude continues to decrease with higher sampling rate as expected.

Sampling Rate	**Worst Phase Error**	**Simulated Noise Amplitude**	**Measured Noise Amplitude**
No compensation	31.25 ps	–	0.7866
40 GHz	25.00 ps	0.5437	0.5217
80 GHz	12.50 ps	0.2816	0.2781
160 GHz	6.25 ps	0.1684	0.1734
320 GHz	3.13 ps	0.0815	0.0942
640 GHz	1.56 ps	0.0533	0.0565
1 THz	1.00 ps	0.0344	0.0436
2 THz	0.50 ps	0.0173	0.0435

Table 1. Calculated and measured noise amplitude after pulse instability compensation at different extrapolated sampling rates.

Figure 4 shows the effects of pulse instability compensation on images formed by delay-and-sum beamforming. The tumor is located at 3 cm to the right from the center, or at coordinate (130, 100). The pulse jitter artifact located at (150,130) is significantly suppressed.

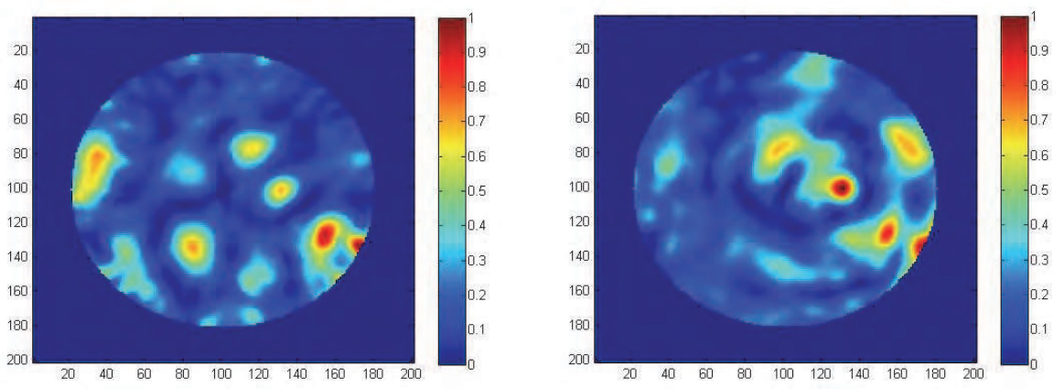

Fig. 4. The effects of pulse instability compensation on breast phantom images. Left: without compensation. Right: with compensation.

3. Real-time oscilloscope

This section discusses the dynamic range of Agilent DSO-081204B real-time oscilloscope used in the experiment. The information of the dynamic range will determine whether the pulse reflected from a tumor is too small to be detected. In this discussion, dynamic range is defined as the ratio of the oscilloscope vertical-scale range and the amplitude of the smallest possible digitized pulse.

Agilent DSO-081204B real time oscilloscope has analog-to-digital converters (ADC) with 8-bit resolution. After averaging and interpolation, the oscilloscope is able to increase the vertical resolution and store the data in 16-bit resolution. Due to quantization of the signal, at least 4-bit resolution is needed to construct the pulse shape of tumor response as shown in Figure 5. So the remaining 12-bit range is the maximum dynamic range of the oscilloscope.

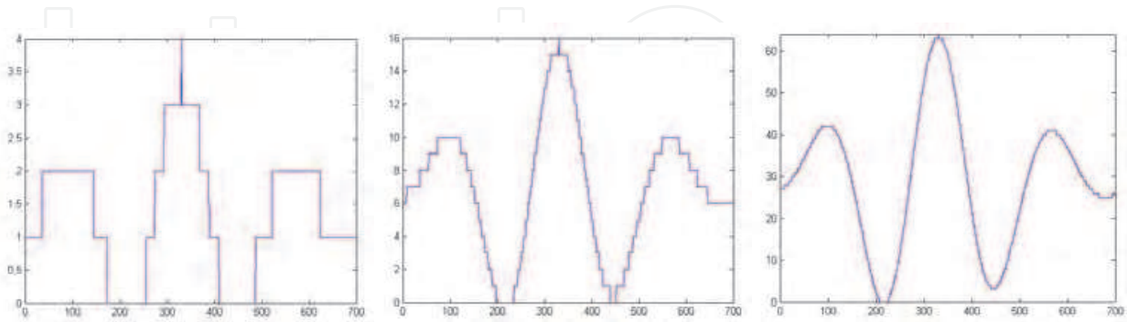

Fig. 5. Ideal tumor response constructed with 2-bit, 4-bit, and 6-bit vertical resolutions showing that the minimum required resolution is 4 bits.

An experiment is conducted to determine the dynamic range of the oscilloscope by investigating its ability to construct a pulse. Due to the presence of noise, a pulse cannot be observed from a single signal. Instead, 360 sets of signals are collected and an averaged

signal is obtained. The random noise will be averaged out, and the pulse can be observed if it is within the dynamic range.
The incident pulse is set very small so that its amplitude is equal to the expected smallest peak for different possible dynamic range as shown in the Table 2. The recorded signals are averaged to determine at which dynamic range the pulse can still be constructed.

$$Expected\ peak = \frac{Full\ range\ voltage}{Dynamic\ range} = \frac{8V}{2^{12}\ bits} = 0.002V \quad (1)$$

From the experiment, , the pulse cannot be seen from the averaged signals if its amplitude is set to 2 mV, while the maximum noise amplitude is 5.9 mV. Whereas for a pulse amplitude of 4mV, the pulse is merely noticeable at sample time 1600 as shown in Figure 6. From this experiment which considers the system noise, the dynamic range is estimated to be 11-bits, which has 2048 values available for the whole range. Thus, the maximum detectable ratio between incident pulse and tumor response is 2048.

Dynamic Range 2^	Smallest peak can be detected	Recorded peak
8bits	31mV	33.2mV
9bits	16mV	14.9mV
10bits	8mV	7.8mV
11bits	4mV	6.1mV
12bits	2mV	5.9mV

Table 2. Expected and recorded peak of incident pulse for different dynamic range.

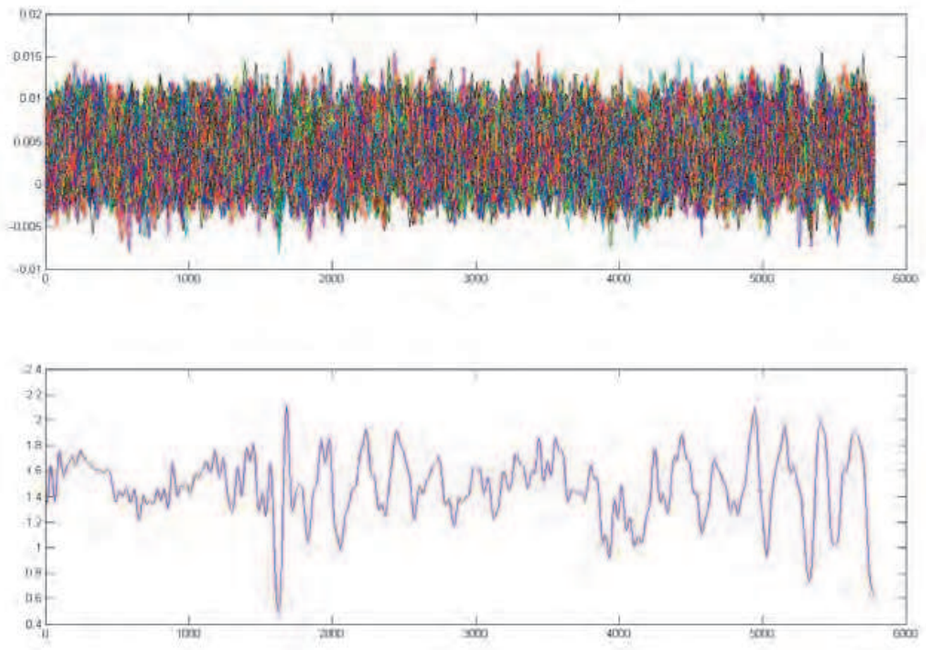

Fig. 6. Constructed pulse to test dynamic range of 2^{11} bits. The pulse is just noticeable at sample 1600. Upper trace shows the 360 signals and lower trace shows the averaged signal.

4. Ring artifact

If the experiments use a breast phantom with higher permittivity, ring artifacts will appear as shown in Figure 7. The phantom is fabricated using tissue mimicking phantom material (Lazebnik, 2005) with 80% oil, contained in a polypropylene cylindrical container (diameter 16cm, height 12cm). The material is able to closely simulate the dielectric properties of human tissues.

Tumor simulant is an 8 mm cube made of phantom material with 10% oil buried at 25 mm right from center of the phantom. The measured dielectric constant at 5 GHz for phantom medium is 9 whereas for tumor is 50 which is representative of normal and malignant human breast tissues. Ring artifacts have not been reported previously by other researchers because their breast phantoms use only lower dielectric constant materials.

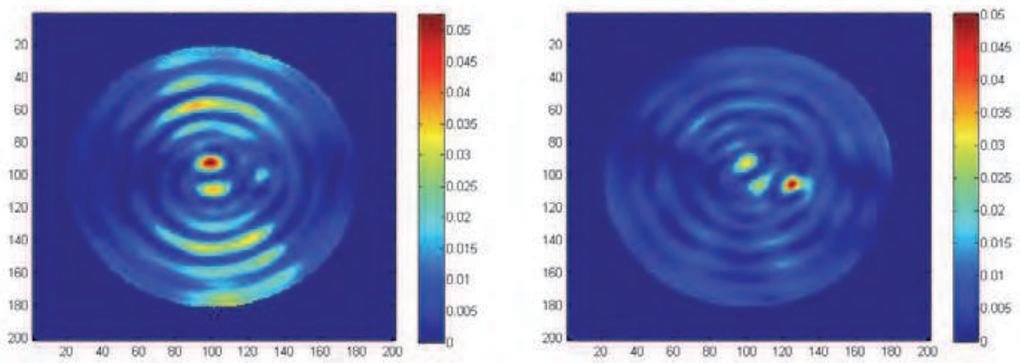

Fig. 7a. Images of breast phantom with 1 mm off-center positioning error (left) and breast phantom less than 0.5 mm off-center error (right).

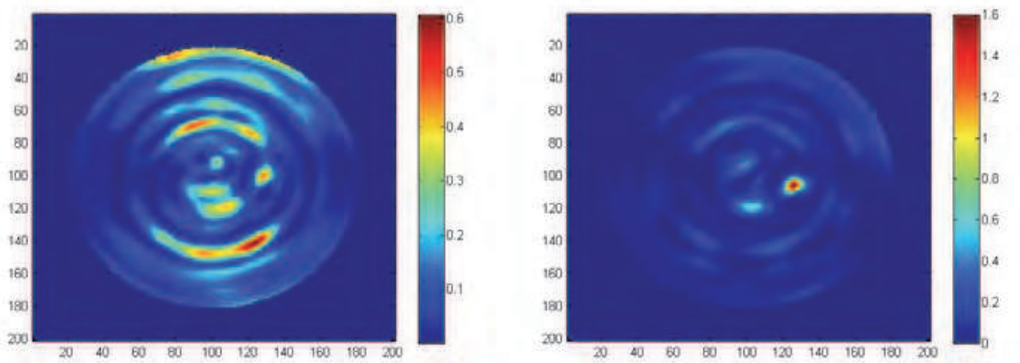

Fig. 7b. Same Images from Figure 7a with correlation applied.

Ring artifact arises from positioning error (off-center) of the breast phantom. Ideally, averaging method works perfectly with round phantom. Ring artifact appears when the phantom is not positioned perfectly on the rotary axis of the experimental stage. This causes small displacement error of the phantom boundary relative to the antennas.

Ring artifact is caused by the coherent adding of the residue boundary reflections after delay-and-sum beamforming. The ring-to-ring distance is proportional to the wavelength of

the incident signal. Ring artifact also indicates the direction of phantom off-center displacement. For instance, when the phantom is displaced to right side, the ring artifact will appear on right indicating positive x-axis off-center displacement and left indicating negative x-axis off-center displacement.
In experiments with oil medium which has lower dielectric constant, ring artifact is not noticeable because the tumor response is large enough to dominate the ring artifacts in the image. The correlation method is not able to improve the image quality when ring artifacts arise as illustrated in Figure 7b. This is due to the high similarity between tumor response and the residue incident pulse ringing.
Adjusting the phantom to the best position using visual inspection will result in a positioning error of 1 mm to 3 mm. Better placement can be achieved by placing a reference object on the antenna to measure the antenna to phantom boundary distance and adjusting the phantom position until the error is smaller than 0.5 mm. The resulting ring artifact is reduced significantly.

4.1 Experiment on ring artifact

An experiment is conducted to test the amplitude of the ring artifact for different displacement errors of a breast phantom without tumor. The phantom is adjusted to the best position with error less than 0.5 mm. Measurements are taken for the phantom at best position, then with off-center displacements of 1 mm, 2 mm, and 3 mm from the best position. The resultant signal artifact shown in Table 3 is computed after applying averaging method. When the breast phantom is perfectly positioned, the signal artifact should be zero.

Position error	Artifact RMS Amplitude ($x10^{-3}$)	Artifact P-P Amplitude ($x10^{-3}$)
<0.5 mm	1.0	2.3
1 mm	3.3	5.7
2 mm	5.5	9.9
3 mm	8.7	15.0

Table 3. Averaged RMS and peak-to-peak amplitude of signal artifact after averaging method for different off-center positioning errors.

5. Loss compensation

This section discusses the power loss during propagation of UWB pulse in breast medium, and the loss models used for compensation. Loss can be contributed by the radial spreading of UWB pulse originating from the antenna as well as attenuation caused by the breast medium. Loss compensation is a signal processing step to equalize all the received signals originating from different locations such that the whole scanning region has unity gain.

5.1 Radial spreading loss

Most studies approximate the propagating signal as a uniform cylindrical wave and thus the radial spreading loss equal to $1/r$, where r is distance from antenna to the particular scanning point. Considering both transmit and receive paths make the loss proportional to distance square. Compensation is done by multiplying the signals by r^2. Figure 8 shows the decrease of reflected signal amplitude from a tumor considering only radial spreading loss. The tumor is located nearest to the antenna at 0 degree and furthest at 180 degrees.

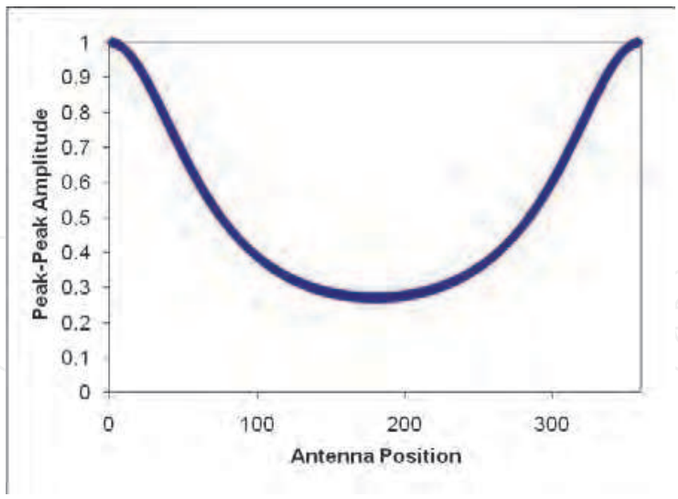

Fig. 8. Simulated received pulse amplitude considering only radial spreading loss.

5.2 Effects of loss compensation

To see the effects of loss compensation, compensation is applied on experiment data to compare the results obtained without compensation applied.

Imaging results in Figure 9 show that loss compensation tends to amplify noise near the phantom boundary. The compensation applied here is only considering radial spreading loss. Worse results will be expected if other loss factors are incorporated, since the signals are multiplied by larger factors.

Radial spreading compensation is a commonly used signal processing step in breast cancer detection algorithms in numerical noise-free modeling. In view of the deteriorating effects of radial spreading compensation on image quality, it is recommended not to apply the compensation.

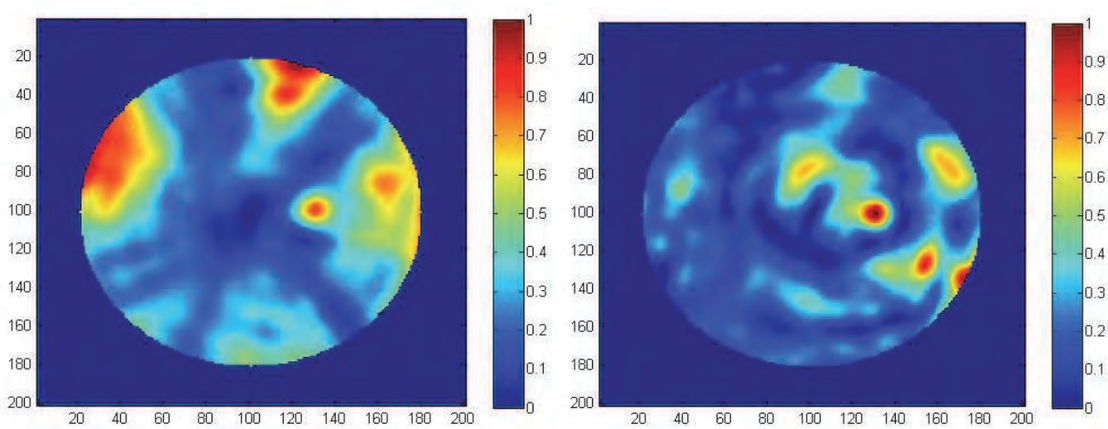

Fig. 9. Image with radial spreading compensation (left) and without radial spreading compensation (right).

6. Filtering and correlation

This section describes two signal processing methods applied to improve the signal-to-noise ratio (SNR) of the breast phantom images.

6.1 Filtering

The ultra-wideband (UWB) antenna used in the experiments has a bandwidth of 1.8 to 6.3 GHz. Two significant narrowband interferences for the experiments conducted are cell phone noise at 1.8 GHz and wireless local area network (LAN) noise at 2.4 GHz. Thus, digital notch filters at 1.8 GHz and 2.4 GHz are applied to reduce the interferences. The signals and power spectra before and after filtering applied are given in Figure 10. The image quality has been improved with filtering as shown in Figure 11.

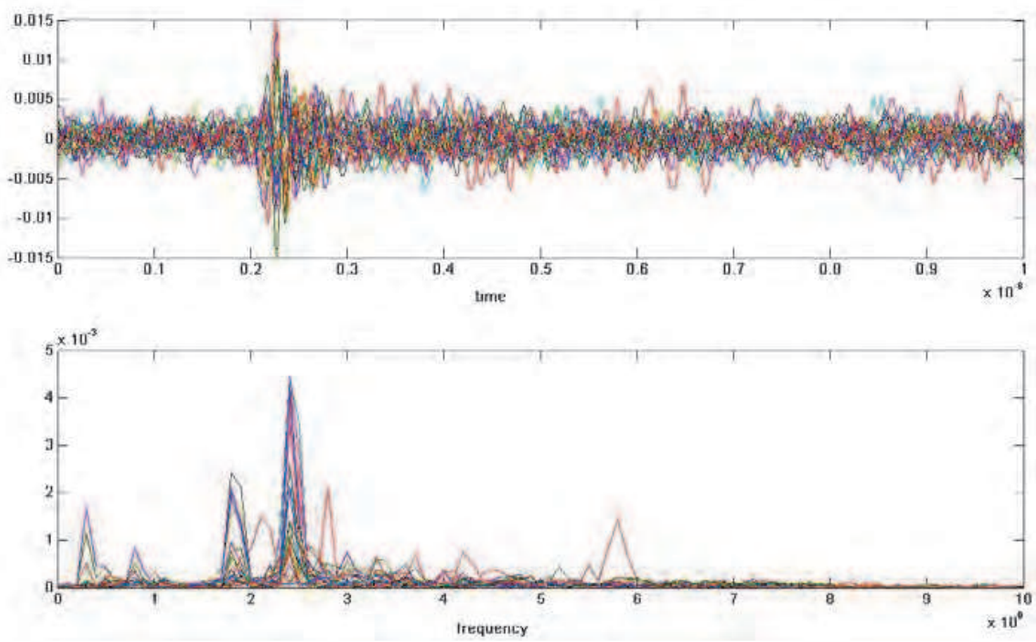

Fig. 10a. Signals (upper trace) and power spectra (lower trace) before filtering.

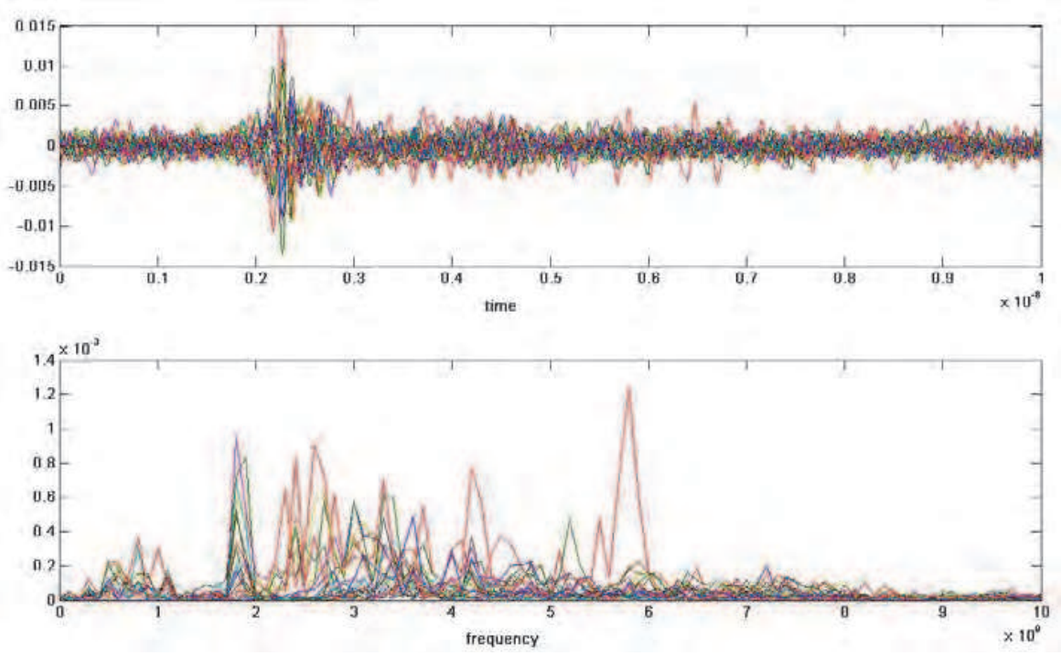

Fig. 10b. Signals (upper trace) and power spectra (lower trace) after filtering.

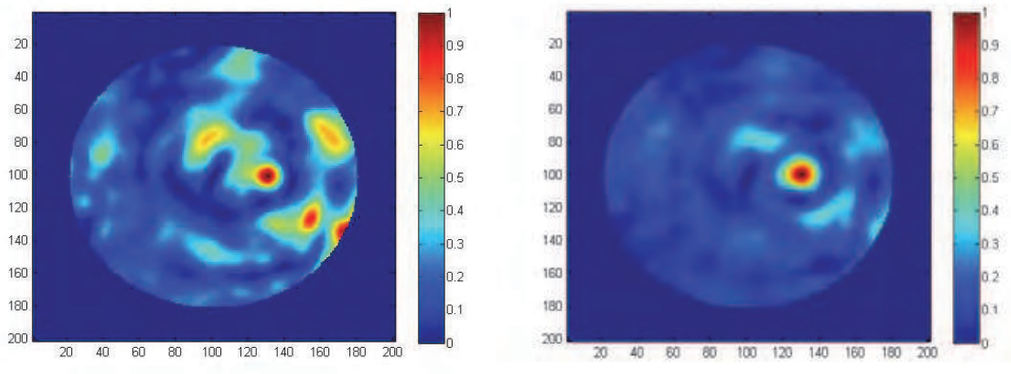

Fig. 11. Images formed without filtering (left) and with filtering applied (right). The tumor is located at 3 cm to the right of the center.

6.2 Correlation

A tumor response template is created in Matlab as shown in Figure 12. Correlation is applied by multiplying the tumor response with the filtered signals after the delay-and-sum operation at each pixel. Then the signals are windowed and summed to give a value for every pixel in the breast phantom image given in Figure 13. The image quality has been enhanced with correlation.

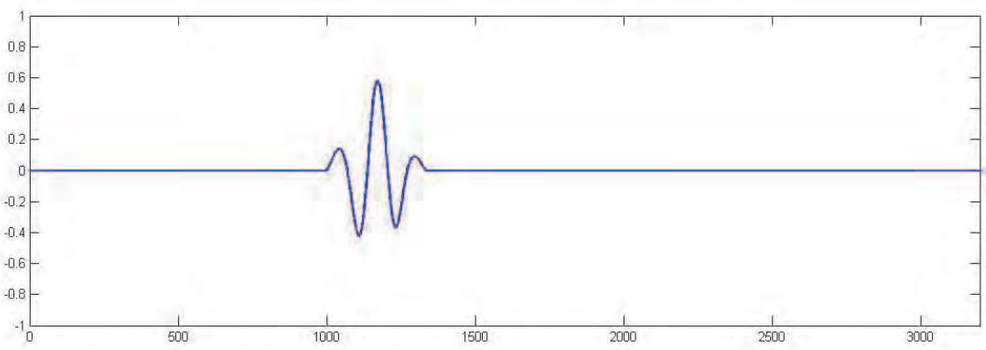

Fig. 12. Tumor response template.

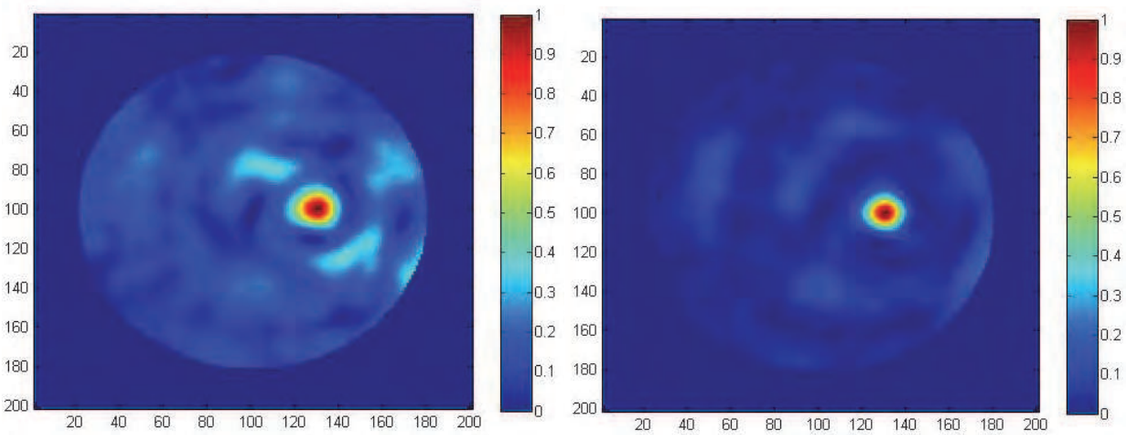

Fig. 13. Comparison for filtered images without correlation (left) and with correlation (right).

The discussion above focuses on only a single experiment data. The result may not be representative as the occurrences of artifacts in images are random due to coherence alignment of noise at certain points. Thus large scale experiments are performed to study the effect of applying filtering and correlation on breast phantom images. Ten experiments are conducted with the same experimental setup and breast phantom. Tumor simulant is at position (130, 100) for all experiments. Experiments are repeated with different antennas array of 6, 12, 24, and 36 elements in one phantom rotation. Forty sets of data are collected and processed. A total of 80 images are formed for SNR analysis. Figure 14 show 20 images from experiments conducted with 24 antennas array.

SNR is calculated from the ratio of the pixel value at tumor location (130, 100) over the highest value of noisy pixels 6 mm radius outside the tumor location. Since the SNR value from individual experiment is highly variable, due to random occurrences of artifacts, an averaged SNR value is calculated using ten SNR values from ten experiments.

Detectability is the ability to observe the tumor in the images although the tumor may not appear as the strongest pixel. Detectability is defined as one when the tumor pixel value is above half of the maximum scale and above twice of the adjacent region pixel values, otherwise zero is given for that image. Table 4 shows that detectability is at least 80% when SNR is positive.

Figure 15 show the SNR versus number of antennas per phantom. There is a significant improvement on SNR with correlation applied. Increasing the number of antennas improves the SNR but cost and complexity of implementation increases. To archive positive SNR, the minimum number of antennas needed without correlation is 12 compared to 10 for correlation.

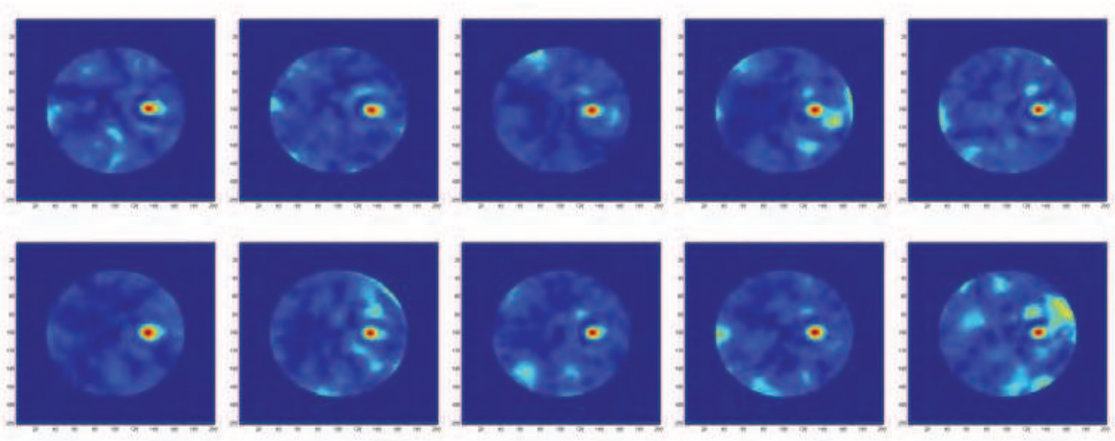

Fig. 14a. Ten filtered images without correlation applied.

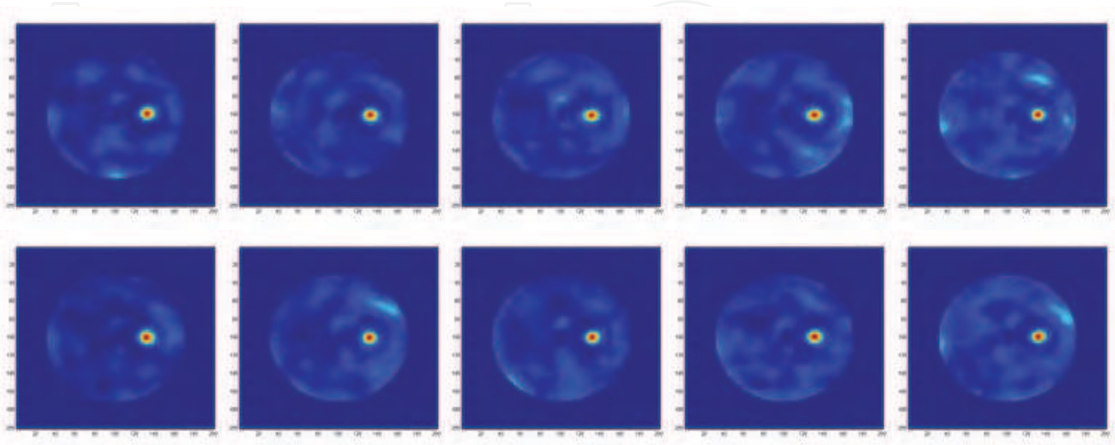

Fig. 14b. Ten filtered images with correlation applied.

SNR	Array of 6	Array of 12	Array of 24	Array of 36
Delay & Sum	-8.7 dB	-3.6 dB	-0.3 dB	4.3 dB
Filtering	-6.3 dB	0.5 dB	6.1 dB	8.2 dB
Correlation	-5.7 dB	3.5 dB	11 dB	13 dB
Detectability	**Array of 6**	**Array of 12**	**Array of 24**	**Array of 36**
Delay & Sum	0/10	5/10	8/10	10/10
Filtering	1/10	8/10	10/10	10/10
Correlation	2/10	10/10	10/10	10/10

Table 4. SNR and detectability for different antennas arrays.

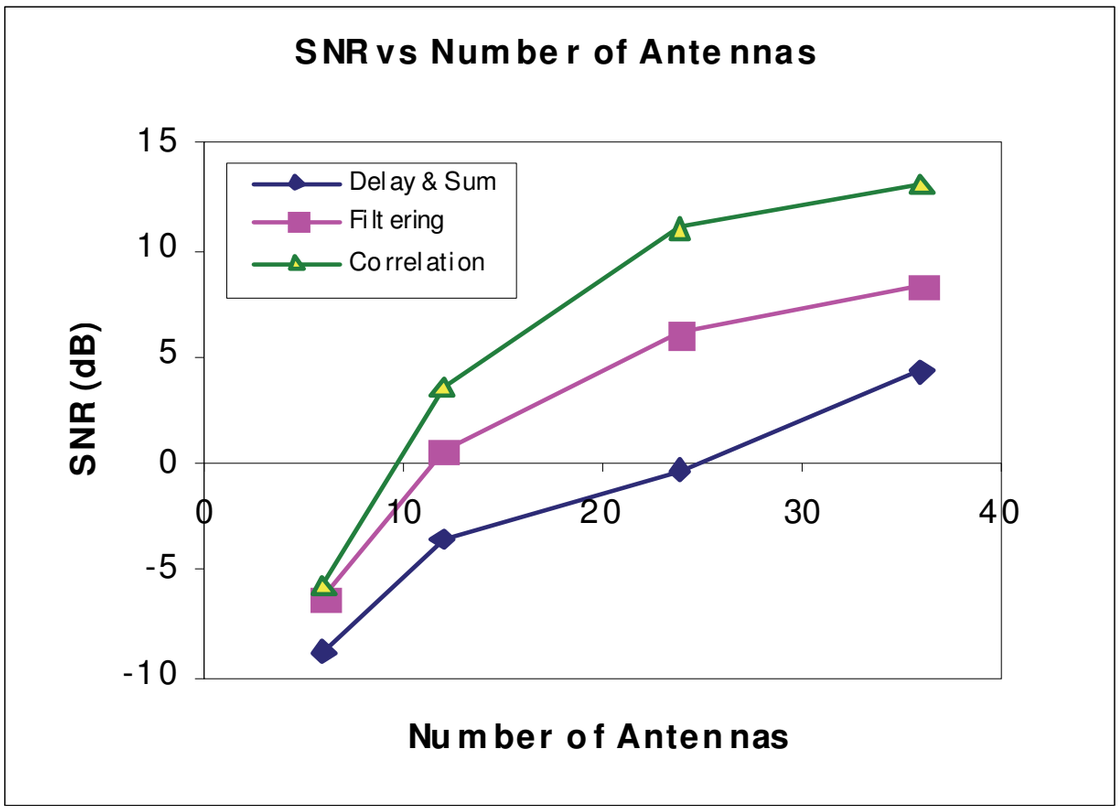

Fig. 15. SNR versus number of antennas.

To study the robustness of the correlation method, the tumor stimulant is positioned at different distances, 1 cm to 6 cm, from the center of the breast phantom with the experimental results given in Figure 16. Images in Figure 16 show that correlation improves the image quality.

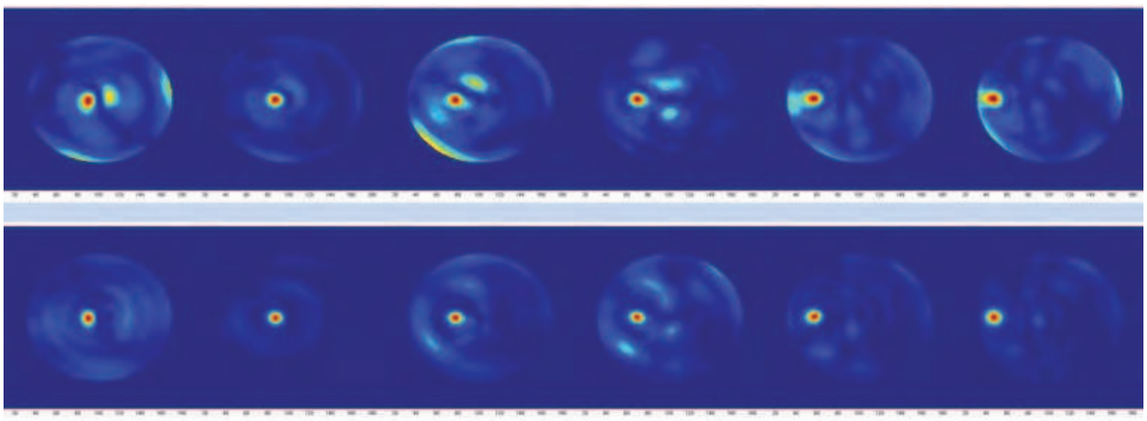

Fig. 16. Images formed without correlation (top) and with correlation (bottom), with tumor located 1 cm to 6 cm from center.

7. Signal and image SNR

This section discusses the effects of improving the image SNR by increasing the averaging number and antenna number. The tradeoff of increasing these two factors is the increase of acquisition time.

In most other studies, an array of only a few antennas are considered as more antennas do not improve the image resolution but at higher simulation time. However, the advantage of more antennas is noise reduction. Better image SNR can be obtained by increasing the averaging number and antenna number.

Some terms used in the discussion are defined as follows:

- Averaging number is the number of waveforms acquired by the oscilloscope to produce an averaged waveform for each acquisition at one antenna position.
- Antenna number is the number of antennas in the synthetic array around the circumference of the phantom. It is also the number of steps for a complete phantom rotation relative to a stationary antenna.
- Signal SNR is the ratio of the root mean square (RMS) value of averaged tumor response to the RMS value of the averaged noise.
- Image SNR is the ratio of the tumor pixel intensity to the highest-value artifact pixel intensity. The definition differs from SCR which is Signal-to-Clutter Ratio, since there is no clutter considered in this discussion. Artifact pixels are caused by coherent summation of noise and occur randomly whereas clutters remain at their positions and averaging is unable to remove them.

7.1 SNR improvement with larger averaging and antenna number

Signal SNR can be improved by using larger averaging number, whereas image SNR can be improved by using larger antenna number.

To measure the noise level, antenna is placed stationary without the presence of breast phantom or any moving object. Incident pulse amplitude is set to different attenuation setting from 0 dB (8 V) to 24 dB (0.5 V). A total of 360 measurements with only incident pulse are taken as in breast scanning. Noise is calculated by subtracting the individual measurement with the average measurements. The RMS and peak-to-peak noise is shown in

Table 5 and Figure 17, which is the average of 360 noise amplitudes relative to the incident pulse amplitude.

Averaging	1	4	16	64	256	1024	4096
RMS noise	4.8 mV	1.7mV	0.83 mV	0.45 mV	0.24 mV	0.15 mV	0.10 mV

Table 5. RMS amplitude of noise for different averaging number with maximum pulse amplitude of 8V (attenuation setting 0 dB).

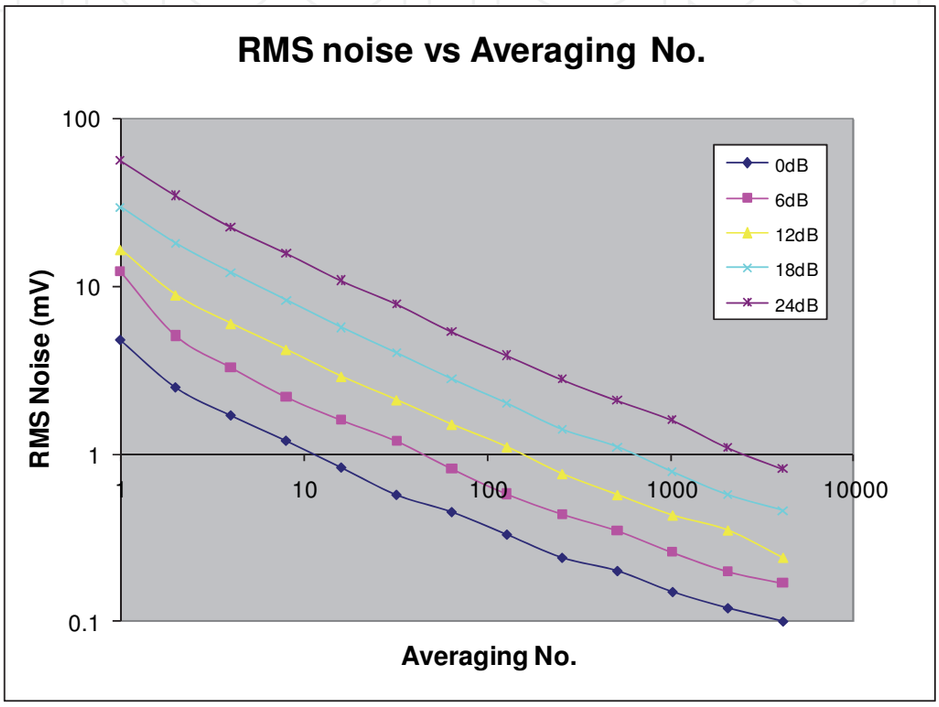

Fig. 17. RMS noise versus averaging number for different pulse attenuation settings.

Matlab simulations are conducted to determine the image SNR. Ten sets of UWB noise are created by applying a bandpass filter to white noise with all the resultant noise RMS amplitudes set to 0.5 mV. The noise is scaled to the noise RMS amplitude of different averaging numbers as shown in Table 5 and added to the ideal tumor response as shown in Figure 12. The tumor response has peak-to-peak amplitude of 1 mV and RMS of 0.2567 mV. The signals are delayed as though they are received from the 360 antennas spaced regularly around the breast phantom. The same delay factors are used in creating the signals and in subsequent beamforming. Thus there is no error caused by delay estimation. A total of 120 sets of data are created for confocal imaging for each antenna number of 12, 24, 45, 90, 180, and 360.

Since the image SNR is random due to random occurrences of artifacts, ten SNR values are obtained and averaged based on simulation with ten sets of data for each averaging number and antenna number. A total of 720 images are produced from the simulations. The results are summarized in Table 6 and Figure 18.

Antenna No.		12	24	45	90	180	360
Averaging No.	**Signal SNR**	**Image SNR**					
2	**-18.66**	-2.8	-2.8	-2.2	-2.4	-2.0	-1.3
4	**-15.89**	-2.8	-2.8	-2.1	-2.1	-1.4	0.0
8	**-13.4**	-2.7	-2.7	-1.9	-1.7	-0.2	1.7
16	**-10.09**	-2.6	-2.2	-1.3	-0.2	1.9	4.0
32	**-7.08**	-2.3	-1.3	-0.2	1.9	4.0	5.8
64	**-4.68**	-1.9	-0.2	1.3	3.8	5.5	6.8
128	**-2.69**	-1.2	1.1	2.6	5.1	6.5	7.5
256	**-0.11**	0.3	2.8	4.4	6.4	7.4	8.1
512	**2.17**	1.9	4.3	5.7	7.2	8.0	8.6
1024	**3.58**	2.9	5.2	6.4	7.7	8.3	8.8
2048	**6.6**	4.8	6.5	7.5	8.4	8.8	9.1
4096	**8.19**	5.6	7.1	8.0	8.7	9.0	9.2

Table 6. Image SNR for different averaging number and antenna number. Signal SNR is calculated with tumor response RMS of 0.2567 mV.

Images from the simulations are shown in Figures 19, 20, and 21 for different sets of noise, noise amplitudes, and antenna numbers. As observed from Figure 18, the cost to increase the image SNR is getting higher when the signal SNR is positive. When the signal SNR is negative, the cost to increase the image SNR is lower. In other word, it is worth using array of more antennas when the tumor response received is weaker than the noise.
In this simulation, the amplitude of the tumor response is fixed at 1 mV, with RMS value of 0.2567 mV. The tumor response is 1000 times smaller than the 1V incident pulse. In this case, we could use antenna number of 12 and averaging number of 1024 to produce reasonably good results.

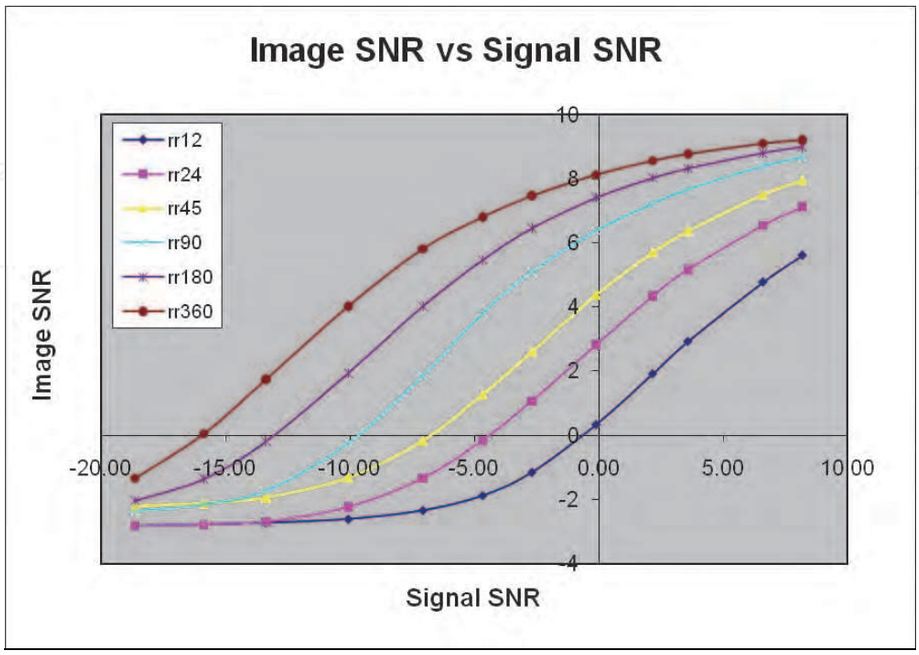

Fig. 18. Image SNR versus Signal SNR for different antenna numbers.

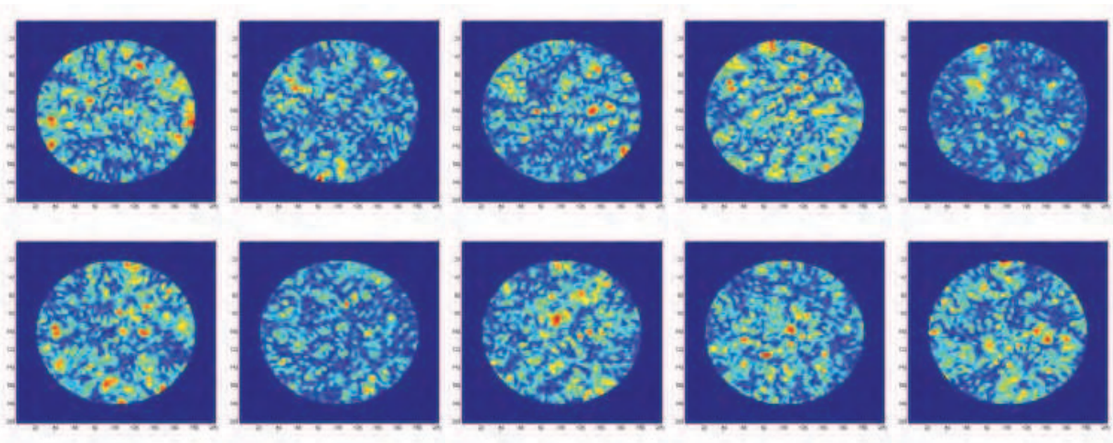

Fig. 19. Images obtained with ten sets of noise processed with antenna number of 360 and RMS noise level of 2.2 mV.

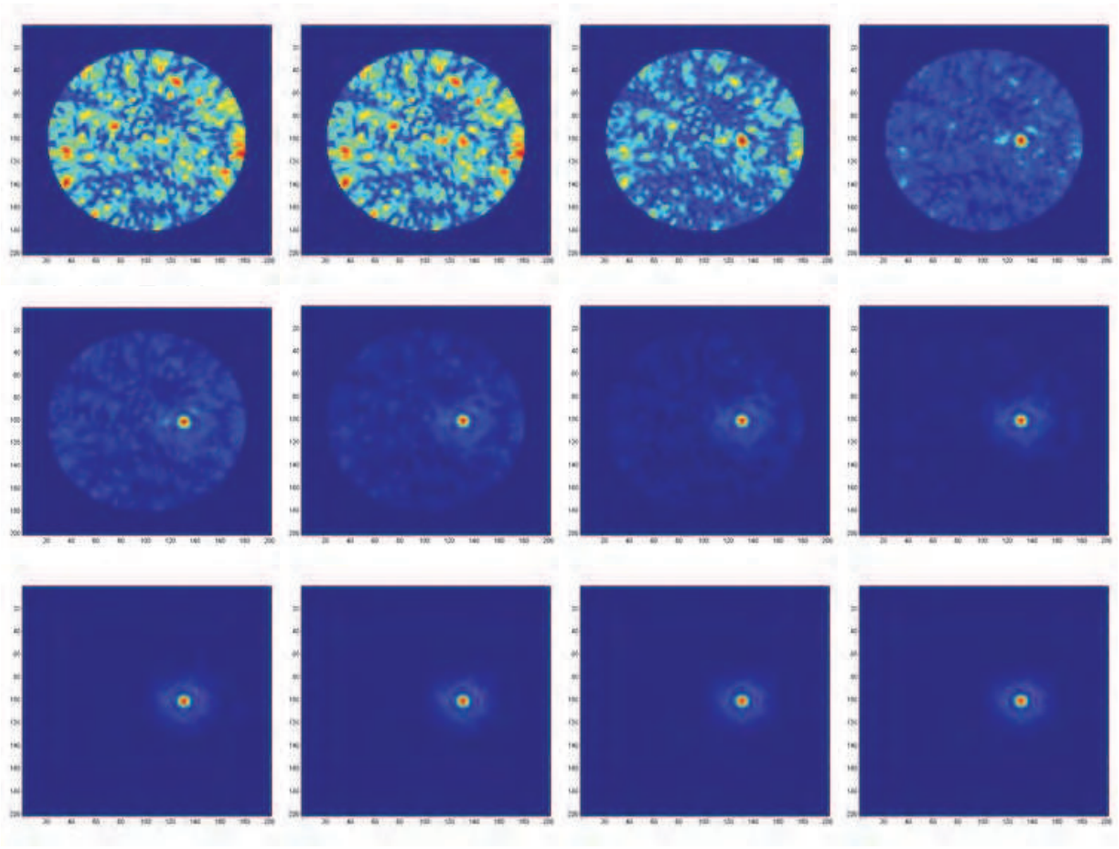

Fig. 20. Images obtained with the same set of noise processed with antenna number of 360 and RMS noise level from 2.2 mV (top left) to 0.10 mV (bottom right).

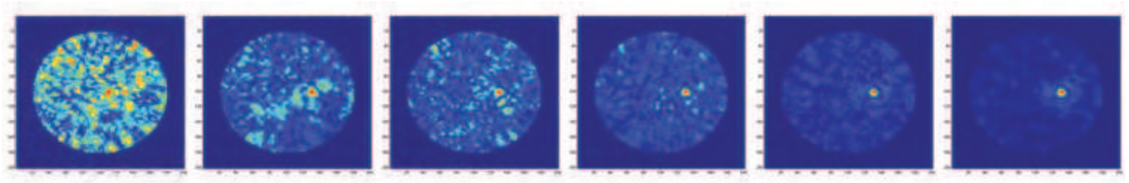

Fig. 21. Images obtained with the same set of noise processed with antenna number of 12 (top left), 24, 45, 90, 180, 360 (bottom right) and RMS noise level of 0.45 mV.

8. Conclusion

In this chapter, experimental study of UWB breast cancer detection in time domain and several important experimental issues are discussed. These include pulse jitter artifact, dynamic range of oscilloscope, ring artifact caused by positioning error, noise amplification caused by radial spreading loss compensation, noise reduction after applying filtering and correlation, as well as the improvement on signal SNR and image SNR by using larger averaging and antenna number. The identified issues and compensation methods will facilitate the future experiments in UWB breast cancer detection with more realistic breast phantoms.

9. References

Bond E. J., Li X., Hagness S. C., & Van Veen B. D. (2003). Microwave Imaging via Space-Time Beamforming for Early Detection of Breast Cancer, *IEEE Transactions on Antennas and Propagation*, vol. 51, no. 8, pp. 1690-1705, ISSN 0018-926X

Chua L. W. (2005). A new UWB antenna with excellent time domain characteristics, *Proceedings of The European Conference on Wireless Technology*, ISBN: 2-9600551-1-X, Paris, October 2005.

Lazebnik M., Madsen E. L., Frank G. R., and Hagness S. C. (2005). Tissue-mimicking phantom materials for narrowband and ultrawideband microwave applications, *Physics in Medicine and Biology*, vol. 50, no. 18, pp. 4245-4258, ISSN 0031-9155

Sill J. M. & Fear E. C. (2005). Tissue sensing adaptive radar for breast cancer detection - experimental investigation of simple tumor models, *IEEE Transactions on Microwave Theory and Techniques*, vol. 53, no. 11, pp. 3312-3319, ISSN 0018-9480

Xu Li & Hagness S. C. (2001). A Confocal Microwave Imaging Algorithm for Breast Cancer Detection, *IEEE Microwave and Wireless Components Letters*, vol. 11, no. 3, pp. 130-132, ISSN 1531-1309

Xu Li, Davis S. K., Hagness S. C., van der Weide D. W., & Van Veen B. D. (2004). Microwave Imaging via Space-Time Beamforming: Experimental Investigation of Tumor Detection in Multi-Layer Breast Phantoms, *IEEE Transactions on Microwave Theory and Techniques*, vol. 52, no. 8, pp. 1856-1865, ISSN 0018-9480

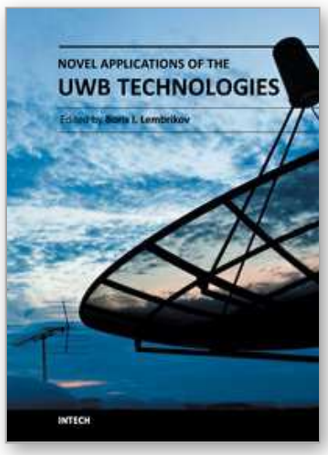

Novel Applications of the UWB Technologies

Edited by Dr. Boris Lembrikov

ISBN 978-953-307-324-8
Hard cover, 440 pages
Publisher InTech
Published online 01, August, 2011
Published in print edition August, 2011

Ultra wideband (UWB) communication systems are characterized by high data rates, low cost, multipath immunity, and low power transmission. In 2002, the Federal Communication Commission (FCC) legalized low power UWB emission between 3.1 GHz and 10.6 GHz for indoor communication devices stimulating rapid development of UWB technologies and applications. The proposed book Novel Applications of the UWB Technologies consists of 5 parts and 20 chapters concerning the general problems of UWB communication systems, and novel UWB applications in personal area networks (PANs), medicine, radars and localization systems. The book will be interesting for engineers and researchers occupied in the field of UWB technology.

InTech Europe
University Campus STeP Ri
Slavka Krautzeka 83/A
51000 Rijeka, Croatia
Phone: +385 (51) 770 447
Fax: +385 (51) 686 166
www.intechopen.com

InTech China
Unit 405, Office Block, Hotel Equatorial Shanghai
No.65, Yan An Road (West), Shanghai, 200040, China
中国上海市延安西路65号上海国际贵都大饭店办公楼405单元
Phone: +86-21-62489820
Fax: +86-21-62489821

IntechOpen